PHYSICAL REVIEW B **81**, 094111 (2010)

Ab initio study of the solubility and kinetics of hydrogen in austenitic high Mn steels

L. Ismer,[1,2,*] T. Hickel,[1,†] and J. Neugebauer[1]
[1]*Max-Planck-Institut für Eisenforschung GmbH, D-40237 Düsseldorf, Germany*
[2]*Materials Department, University of California, Santa Barbara, California 93106-5050, USA*

(Received 18 December 2009; revised manuscript received 15 February 2010; published 22 March 2010)

Chemical trends for the solubility and diffusivity of hydrogen in austenitic high Mn steels have been studied employing density-functional theory. Considering the dilute limit of hydrogen, we observe strong volumetric effects of substitutional Mn and interstitial carbon on the energetics of a hydrogen atom within the lattice. This volume dependence yields a significant increase both in the solubility and the mobility of the H impurity when comparing $Fe_{1-x}Mn_xC_y$ with pure Fe. By means of kinetic Monte Carlo calculations, we also show that H impurities can use Mn percolation chains as efficient diffusion channels. These trends may explain why Mn-rich steels are often observed to be more prone to hydrogen embrittlement than conventional austenitic steels.

DOI: 10.1103/PhysRevB.81.094111 PACS number(s): 71.15.Nc, 71.15.Pd, 66.30.J−, 61.72.J−

I. INTRODUCTION

High manganese steels containing 15–25 wt % Mn exhibit exceptional properties with respect to strength and plasticity, which make them a promising material system for light-weight constructions. Several applications, in particular, in automotive industry are foreseen[1] and extensive research on Fe-Mn has been started in recent years.[2,3] Previous investigations revealed the relation of the high work-hardening rates and the ductility to microstructural mechanisms in these austenitic steels.[4] In contrast to ferritic steels, the high Mn content ensures that the material adopts the fcc crystal structure (γ phase) under normal conditions. Under mechanical load, this structure is fully modified,[2–4] and depending on the stacking-fault energy, it either experiences extensive twin formation (TWIP—twinning-induced plasticity), which act as obstacles for dislocation gliding or performs multiple martensitic transformations (TRIP—transition-induced plasticity) resulting into ε (hcp) and α' (bcc) phases in the γ (fcc) matrix.[5,6]

The mechanical properties are in addition influenced by failure mechanisms occurring in these materials. In particular, hydrogen embrittlement (HE) is a potential candidate for the formation and growth of cracks and might also limit the applicability of high Mn steels. Austenitic steels are often considered to be immune to HE, due to their low H permeability and the elevated capacity to dissolve H, which are both inherently connected to the fcc crystal structure of the austenitic phase.[7] Both, the permeability and the solubility, are expected to strongly affect the time scale in which a critical concentration of hydrogen can be transferred into strained regions of inhomogenously deformed materials and can thus contribute to crack growth and eventually to embrittlement. In contrast to this picture, already in 1940s, a strong influence of H on the mechanical properties of some Hadfield steels (containing 12–14 at. % Mn) has been observed.[8] More recently, it has been shown for a Fe-Mn-Al alloy containing 17 at. % Mn that austenitic high Mn steels may be prone to H degradation (see Ref. 9, and references therein) and that some austenitic steels, depending on the chemical composition, exhibit significant hydrogen-enhanced crack growth.[10,11]

There have been a large variety of possible explanations for HE in austenitic steels. Lattice decohesion (e.g., Ref. 12), formation of pseudohydrides (e.g., Ref. 13), and hydrogen-enhanced localized plasticity (e.g., Ref. 14) have been proposed. Intergranular fracture was also suggested to be related to a trapping of hydrogen at the grain boundaries or the formation of a strain-induced martensite phase.[10,11] However, it remains unclear which (combination) of these effects is decisive for HE.

Nevertheless, it is now undoubted that despite their principally low H permeability, austenitic steels are under certain conditions affected by HE and that the chemical composition is an important criterion in this context. This finding is supported by the observation that the nickel content is one of the main parameters to meet HE resistance.[15–17] Also silicon increases the ductility of hydrogen-charged austenitic steels.[18] For manganese, however, such a systematic positive (or negative) influence on HE has not been reported so far. A comparative experimental study[19] showed, for a particular steel with a high Mn content, an increased hydrogen solubility.

The aim of this study is to reveal to what degree the chemical composition of TRIP and TWIP steels, i.e., in particular, the Mn and the C content, influences the two key quantities related to HE, which have been mentioned above: the hydrogen solubility and diffusivity. Such an analysis, though highly desired,[15] is hard to perform experimentally due the inevitable interplay of the various chemical species as well as the strong influence of the microstructure. The theoretical approach of density-functional theory (DFT), instead, is very well suited to systematically understand fundamental trends intrinsically connected to the chemical composition of the steel. It allows the consideration of perfect crystals containing no further perturbation and the derivation of its properties from the first principles of quantum mechanics. In this way, one can separate the pure chemical effect from the variety of further HE mechanisms.

Most DFT studies on interstitial impurities conducted so far focused on the α phase of iron,[20–23] do not treat interstitial hydrogen,[24] or do only consider pure iron, without alloying.[25] A systematic study of hydrogen in γ iron is still missing and information on the influence of alloying ele-

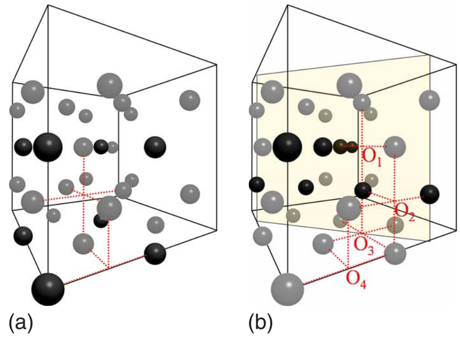

FIG. 1. (Color online) A $\mathrm{Fe}_{24}\mathrm{Mn}_8$ supercell with the Mn (dark gray balls) atoms arranged (a) at a cubic superlattice and (b) in connected (percolation) chains. The red dotted lines display inequivalent octrahedral sites and the shaded area highlights the [110] plane that is used in Fig. 4.

ments (such as, e.g., Mn) and interstitial impurities (such as, e.g., C) are not yet available. After some computational details about our DFT approach in Sec. II, we will in Sec. III therefore start with an investigation of fcc Fe, before taking step by step these two alloying elements as well as effects of magnetism and zero-point vibrations (ZPVs) into account. The derived conclusions will be summarized in Sec. IV.

II. COMPUTATIONAL DETAILS

Both, the solubility of hydrogen and its diffusion constant in the dilute limit are determined by the energy necessary to incorporate a single hydrogen atom in certain interstitial positions of the metal. The host material has been modeled by means of a cubic fcc supercell containing N_{at} atoms. As an initial test system, the pure Fe matrix is used and the impact of substitutional Mn (see Fig. 1) and interstitial C in this supercell has been studied.

The energy for putting a hydrogen atom at a certain site σ in the metal M defines the solution enthalpy,

$$H^f_\sigma = E_{\mathrm{M}_{N_{\mathrm{at}}}\mathrm{H}}[\sigma] - (E_{\mathrm{M}_{N_{\mathrm{at}}}} + E_{\mathrm{H}}), \tag{1}$$

where the reference is given by the total energy per supercell of the unperturbed host metal lattice and the energy of a single hydrogen atom outside the metal (half the energy of a H_2 molecule). Sievert's law states that for low concentrations, the hydrogen concentration c_σ for a certain type of sites σ is, to a good approximation, given by

$$c_\sigma \sim \sqrt{p}\,\exp\left(-\frac{H^f_\sigma}{k_{\mathrm{B}}T}\right). \tag{2}$$

Here, p is the pressure, k_{B} is the Boltzmann constant, and T is the temperature. Hence, the total hydrogen concentration is described by an Arrhenius law with a temperature dependence, mainly determined by the smallest solution enthalpy H^f_{min} of hydrogen in the host material.

Further, the energy of hydrogen at the transition point, i.e., the highest-energy point along the minimum-energy pathway between two neighboring minima, defines the diffusion barrier,

$$E^{\mathrm{diff}} = E_{\mathrm{M}_{N_{\mathrm{at}}}\mathrm{H}}[\mathrm{trans}] - E_{\mathrm{M}_{N_{\mathrm{at}}}\mathrm{H}}[\mathrm{min}]. \tag{3}$$

In transition state theory, the diffusion barrier E^{diff}_{ij} determines the rate of an H atom to jump between these two neighboring sites i and j via

$$\Gamma_{ij} = \nu\,\exp\left(-\frac{E^{\mathrm{diff}}_{ij}}{k_{\mathrm{B}}T}\right). \tag{4}$$

Here, Γ_{ij} is the hopping rate between the lattice sites i and j, and ν is the attempt frequency, for which the characteristic frequency of an LO-TO phonon ($10^{13}\ \mathrm{s}^{-1}$) is chosen in this work. The diffusion process is mathematically described by a master equation,

$$\frac{\partial P_i(t)}{\partial t} = \sum_j \{P_j(t)\Gamma_{ji} - P_i(t)\Gamma_{ij}\}, \tag{5}$$

where $P_i(t)$ is the probability of finding the H atom at time t on lattice site i, and is simulated by kinetic Monte Carlo (KMC) simulations in this work. The diffusivity of hydrogen D_{H} in the host metal is determined from the mean-square displacement of the H atom from its original site during the KMC simulation (Einstein expression). For the system considered here, the resulting value follows again an exponential dependence. This computed dependence is used to derive an effective barrier energy E^{eff},

$$D_{\mathrm{H}} \sim \exp\left(-\frac{E^{\mathrm{eff}}}{k_{\mathrm{B}}T}\right). \tag{6}$$

All total energies in Eqs. (1) and (3) have been obtained from DFT calculations using the generalized gradient approximation[26] to describe electronic exchange and correlation interactions. The projector-augmented waves[27] approach, as implemented in VASP,[28] has been employed. The calculations have been performed with a plane-wave cutoff energy of 270 eV and two different k-point sets for the sampling of the electronic Brillouin zone. For the calculation of the absolute values of the solution enthalpy in Fe, FeMn, Mn, and $\mathrm{Fe}_{32}\mathrm{C}$, a k-point sampling with a $8\times8\times8$ Monkhorst-Pack mesh for a cubic fcc supercell containing 32 metal atoms was needed to achieve the targeted accuracy of 10 meV for the solution enthalpies and migration barriers. For energy differences, such as the potential-energy surfaces in FeMn and $\mathrm{Fe}_{32}\mathrm{C}$, a k-point sampling with a $6\times6\times6$ Monkhorst-Pack mesh was found to be sufficient. For the electronic occupation numbers, a first-order Methfessel-Paxton scheme with a smearing of 0.1 eV has been used. Atomic relaxations have been performed using a second-order quasi-Newton scheme. Convergence has been checked by determining the total-energy difference between subsequent atomic relaxation steps. The calculation has been considered to be converged when this difference was smaller than 1 meV.

The dilute limit is a suitable approximation for the situation in the austenitic bulk metal and ensures well-defined quantities. To avoid the interaction of H atoms in adjacent supercells, size convergence of the supercell has to be checked. As Table I shows for the example of H at the octahedral site, a $2\times2\times2$ supercell containing 32 metal atoms

TABLE I. Dependence of the H-solution enthalpy (calculated at constant pressure $p=0$) at the octahedral site O of nonmagnetic γ Fe as a function of the supercell size. All energies in electron volt.

	Fe_4H	$Fe_{32}H$	$Fe_{108}H$
$H^f_{\mathrm{O}}[p=0]$	0.13	0.06	0.04

yields an error on the order of 20 meV. For diffusion barriers and also for the comparison between Fe and Mn and FeMn, this artificial contribution largely cancels out and is smaller than 10 meV in a 2×2×2 supercell. The energies $E_{\mathrm{M}_N\mathrm{H}}[\mathrm{min}]$, $E_{\mathrm{M}_N\mathrm{H}}[\mathrm{trans}]$, and E_{M_N} are calculated at constant pressure, $p=0$, to optimize supercell convergence.

Corrections to the solution enthalpy arising from quantum-mechanical zero-point vibrations have been considered for representative configurations and are discussed in Sec. III. These calculations have been performed within the harmonic approximation in a Fe_{32} cell by diagonalizing the corresponding real-space dynamical matrix. The latter has been constructed by computing symmetric two-step finite differences using a displacement of ±0.01 Å.

III. RESULTS

A. H in nonmagnetic fcc Fe

In order to understand how alloying elements affect hydrogen solubility and kinetics, the respective properties in pure Fe need to be determined first. In the same spirit and to reveal underlying trends, the impact of magnetism and lattice vibrations will only be considered in a second step (Sec. III D). Based on this decomposition, we calculated the hydrogen formation energy for various interstitial configurations (Fig. 2). The corresponding results are summarized in Table II. The lowest solution enthalpy is observed for the octahedral site whereas the tetrahedral site is energetically less favorable by 0.43 eV. This behavior can be geometrically explained by considering the energies provided in the third row of Table II. The energy related to the relaxation of the host lattice when incorporating hydrogen turns out to be much larger for the tetrahedral site than for the octahedral site. Since the octahedral void has a larger volume, the obtained H-Fe bond length for this configuration is apparently already in the unrelaxed case closer to the optimal value, resulting in a lower value for the solution enthalpy.

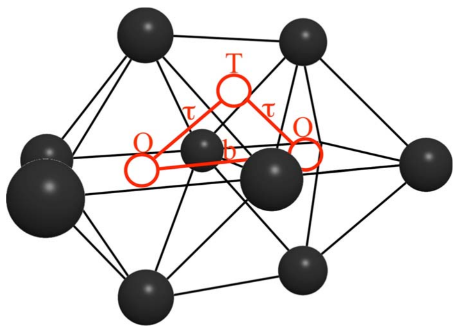

FIG. 2. (Color online) High-symmetry interstitial sites (red) for the incorporation of H into an fcc host lattice (dark balls). The octahedral/tetrahedral site are labeled "O" and "T," respectively. Two possible diffusion paths between adjacent octahedral sites are marked with red lines and their saddle points are labeled "τ" and b.

TABLE II. Selected H-solution enthalpies [Eq. (1), excluding zero-point vibrations and calculated at constant pressure $p=0$] in a nonmagnetic γFe_{32} supercell at different interstitial sites σ (see Fig. 2), both as absolute values and with respect to the octahedral site. The enthalpies include atomic relaxation (rel.). The energy gained by the system due to the relaxation of the host Fe lattice is given in the last row. All energies in electron volt.

	O	T	τ	b
$H^f_{\sigma}[p=0]$	0.06	0.50	0.68	1.12
$H^f_{\sigma}[p=0]-H^f_{\mathrm{O}}[p=0]$	0.00	0.44	0.62	1.06
$H^f_{\sigma}[\mathrm{unrel.}]-H^f_{\sigma}[\mathrm{rel.}]$	0.18	0.66	1.01	2.18

In order to calculate the diffusivity in fcc Fe, the lowest-energy pathway connecting two octahedral sites is determined. The direct path via the bond-center site "b" (Fig. 2) is connected with an energy barrier of more than 1 eV (Table II). In contrast to that a diffusion path via the tetrahedral site is energetically much more favorable. The corresponding transition point, labeled τ, is characterized by a threefold coordination of nearest-neighbor Fe atoms to the hydrogen atom. The lower energy of the diffusion barrier for the second path can again be explained geometrically, as also indicated by the relaxation energies provided in Table II.

B. Effect of substitutional manganese

The fcc crystal structure of steels is stabilized by a certain amount of Mn. Irrespective of the presence of the fcc phase throughout the crystal, the Mn content still shows stochastic fluctuations, which might have an influence on the hydrogen solubility. As a limiting case, we consider at first the situation that the local neighborhood of H solely consists of Mn atoms. For this purpose, we performed at first calculations with supercells where all Fe atoms (in the previously considered fcc cell) have been substituted by Mn. To estimate the effect of local strain, the calculations are performed for a set of lattice constants. The results are summarized in Table III and show a clear reduction in the diffusion barrier as well as the

TABLE III. Bulk equilibrium lattice constants, H-solution enthalpies [Eq. (1)], and H-diffusion barriers [Eq. (3)] in nonmagnetic fcc Fe, Mn, and in the $Fe_{24}Mn_8$ structure shown in Fig. 1(a). The solution enthalpies and diffusion barriers have been calculated in supercells containing 32 host metal atoms at constant volume (corresponding to the given bulk lattice constants). Lattice constants are in angstrom and energies are in electron volt.

	Fe	Mn	$Fe_{24}Mn_8$
a_{lat}	3.447	3.497	3.458
H^f_{O}	0.07	−0.03	0.05
E^{diff}	0.62	0.55	0.58

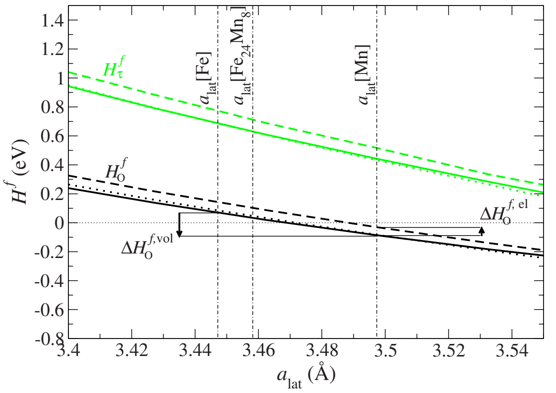

FIG. 3. (Color online) H-solution enthalpies at the octahedral interstitial lattice sites (black lines) and at the transition states for hydrogen diffusion (light, green lines), plotted as a function of the lattice constant, for Fe (solid lines), Mn (dashed lines), and the highly ordered Fe$_3$Mn alloy given in Fig. 1(a) (dotted lines). The vertical dot-dashed lines give the theoretical bulk lattice constants of the three different structures. $\Delta H^{f,el}_\mathrm{O}$ and $\Delta H^{f,vol}_\mathrm{O}$ mark the electronic and the volumetric contributions to the difference in the H-solution enthalpy between Fe and Mn [Eqs. (8) and (9)].

solution enthalpy. This behavior can be understood by analyzing the difference in the solution enthalpy, ΔH^f_O, in detail. We decompose it into, first, a contribution induced by changing the volume (a_lat=3.497 Å in Mn whereas a_lat=3.447 Å in Fe) and, second, a contribution related to the change in the electronic structure (Mn has one 3*d* valence electron less than Fe),

$$\Delta H^f_\mathrm{O} = H^f_\mathrm{O}[\mathrm{Fe}] - H^f_\mathrm{O}[\mathrm{Mn}] = \Delta H^{f,vol}_\mathrm{O} + \Delta H^{f,el}_\mathrm{O}. \tag{7}$$

Here

$$\Delta H^{f,vol}_\mathrm{O} = H^f_\mathrm{O}[\mathrm{Fe}, a_\mathrm{lat}(\mathrm{Fe})] - H^f_\mathrm{O}[\mathrm{Fe}, a_\mathrm{lat}(\mathrm{Mn})] \tag{8}$$

is the difference between the H-solution enthalpies in Fe at the Fe and at the Mn equilibrium lattice constant, respectively, and

$$\Delta H^{f,el}_\mathrm{O} = H^f_\mathrm{O}[\mathrm{Fe}, a_\mathrm{lat}(\mathrm{Mn})] - H^f_\mathrm{O}[\mathrm{Mn}, a_\mathrm{lat}(\mathrm{Mn})] \tag{9}$$

is the difference in the H-solution enthalpies between Fe and Mn at the equilibrium lattice constant of Mn. These definitions are not unique since one could take the volume term for Mn (instead of Fe) or calculate the electronic term at the Fe equilibrium lattice volume (instead of the Mn lattice constant). However, using our actual data both definitions give almost identical results.

Using the decomposition [Eq. (7)], the two contributions are indicated in Fig. 3 and listed in Table IV. We find that the volume contribution dominates (it is roughly three times larger than the electronic contribution) and that both have an opposite effect on the solution enthalpy: While an increase in the volume reduces the H-solution enthalpy, the change in the electronic structure when replacing Fe by Mn increases it. Similar trends are found for the diffusion barrier. We therefore conclude that the differences in the interaction with interstitial H between Fe and Mn are dominated by volumetric effects. The larger lattice constant of Mn provides a larger interstitial embedding volume for the hydrogen atoms.

TABLE IV. Decomposition of the difference between the formation energy of interstitial hydrogen in Fe and Mn [see Eqs. (7)–(9) and Fig. 3]. All energies in electron volt.

ΔH^f_O	0.10
$\Delta H^{f,vol}_\mathrm{O}$	0.15
$\Delta H^{f,el}_\mathrm{O}$	−0.05

In a next step, we consider Fe-Mn alloys. We here focus on alloys with a Mn concentration of 25 at. % since this is the range of realistic high manganese steels. Rather than studying a large number of possible local atomic configurations around the interstitial H atom, we restrict our discussion on two configurations that represent extreme cases with respect to the local arrangement of the Mn atoms. A key insight of the following analysis will be that these two extreme configurations follow the same quantitative relations as the pure Fe and Mn results (see, e.g., Fig. 5). Thus, the two cases considered in the following are expected to cover the main trends of the interaction of H with FeMn alloys.

The first configuration we investigate is the highly symmetric structure shown in Fig. 1(a), where the Mn atoms are arranged in a cubic superlattice. This configuration corresponds to the largest separation of Mn atoms within the given supercell. The Mn substitution lowers the fcc symmetry of the Fe lattice, yielding two symmetry-inequivalent octahedral sites [indicated by the crosses in Fig. 1(a)]. Placing H on these sites yielded solution enthalpies that are energetically degenerate within the numerical accuracy of our calculation (~5 meV). The obtained values for the H-solution enthalpy and the diffusion barrier of this alloy (dotted lines in Fig. 3), calculated at the theoretical equilibrium lattice constant a_lat=3.458 Å are significantly lower (respectively, by 0.02 eV and 0.04 eV, see Table III) than the corresponding values for an Fe crystal. We can, therefore, conclude that the increase in the equilibrium volume due to the presence of Mn yields a noticeable reduction in the solution enthalpy and the diffusion barrier. It is, moreover, interesting to note that the energy-volume curves (Fig. 3) for the solution enthalpy in the Fe$_3$Mn alloy at the octahedral site and at the transition state almost perfectly coincide with those corresponding to pure Fe (solid vs dotted line). We therefore conclude that for this specific alloy, the main impact of the Mn incorporation is to increase the alloy lattice constant. Changes in the electronic structure have, for this Mn concentration, practically no effect on the hydrogen energetics.

To understand whether this behavior is a consequence of the highly ordered alloy considered here or whether it is a generic property of FeMn alloys, we consider next a supercell with another distribution of the Mn atoms than in Fig. 1(a). From percolation theory,[29] it is known that on a fcc lattice, the site percolation threshold is 0.1992, i.e., above a critical Mn concentration of ≈20%, chains of neighboring Mn atoms penetrate through the entire FeMn crystal. These chains may be relevant for the diffusion of hydrogen in disordered FeMn alloys with a Mn content of more than 20%. We will therefore consider next an alternative Fe$_3$Mn alloy that contains percolation chains as sketched in Fig. 1(b). One

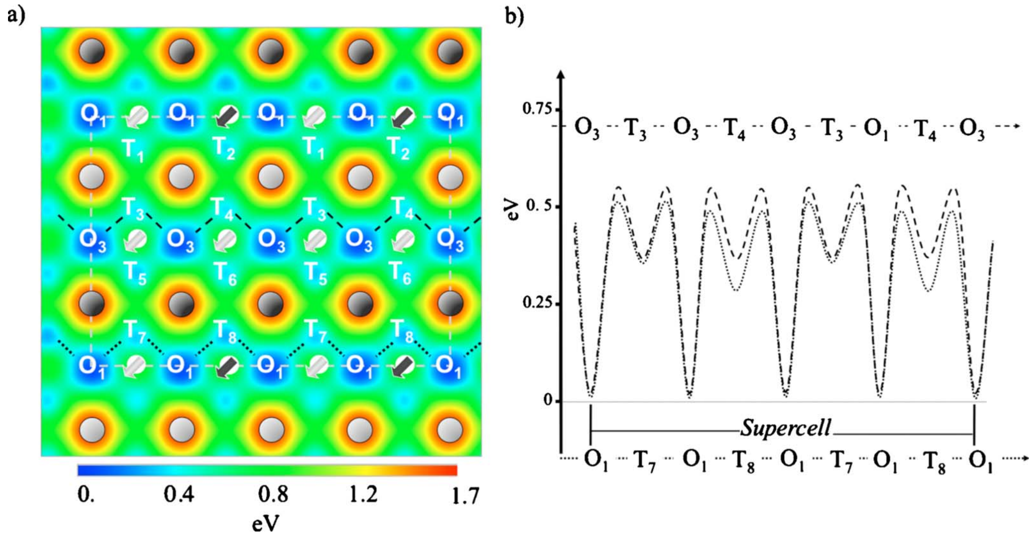

FIG. 4. (Color online) (a) Potential-energy surface (colored, schematic) for placing a hydrogen atom along the [110] plane of a Fe_3Mn supercell with a chainlike arrangement of Mn atoms as sketched in Fig. 1(b). The dark (light) balls denote the positions of the Mn (Fe) atoms. The octahedral (tetrahedral) interstitial lattice sites are labeled O_x (T_x). The dark (light) arrows denote the direction to out-of-plane nearest-neighbor Mn (Fe) atoms. The dashed lines denote specific paths for hydrogen diffusion. (b) Solution enthalpies and energy barriers along the dotted ($O_1 \cdots T_7 \cdots O_1 \cdots T_8$) and the dashed ($O_3 \cdots T_3 \cdots O_3 \cdots T_4$) path marked in (a). All energies are in electron volt and are taken with respect to the lowest-energy position for H and the O_1 octahedral site.

of these chains has a nearest-neighbor Mn connectivity along [110] and the other along $[1\bar{1}0]$. The formation energy of such a configuration is slightly higher in energy (by 0.06 eV per Mn atom) than the corresponding energy of the cubic superlattice.[30]

For this configuration, a substantial dependence of the H-solution enthalpy on the surrounding atoms was observed. We have, therefore, mapped the complete three-dimensional (3D) potential-energy surface (PES) for H in this supercell. A two-dimensional (2D) cross section of this PES is shown in Fig. 4. The total-energy minimum was observed for the O_1 octahedral site [see Fig. 1(b)], i.e., at the intersection of the two percolation chains. The solution enthalpy at this position is significantly lowered as compared to the highly ordered Fe_3Mn alloy in Fig. 1(a) (by 0.02 eV) and pure Fe (by 0.04 eV). The energy on this site is also lower than on octahedral sites further away from the percolation chains as, e.g., O_4 (the corresponding energies are listed in the table included in Fig. 4).

A closer analysis showed an approximate inverse correlation between these solution enthalpies and the number of nearest-neighbor Mn atoms of the particular site. In order to quantify these effects, we have determined the net volumes of octahedral interstitial voids O_x in the absence of H employing a Voronoi construction. The results are summarized in Fig. 5 and show a clear correlation between the local interstitial volume and the solution enthalpy of a void. An interesting consequence of this finding is that interstitial H in high Mn steels preferentially aggregates at Mn percolation chains due to local volumetric effects.

In addition to the energy minima, the 3D potential-energy surface provides direct insight into the diffusion behavior in the presence of percolation chains. In the 2D plot of Fig. 4(a), two diffusion paths along a connected chain of Mn atoms are indicated (dashed and dotted lines). From Fig. 4(b) and the bottom table, we find that the highest diffusion barrier along these paths is 0.51 eV and 0.53 eV, respectively. These values are considerably lower than the diffusion barrier in pure Fe, in the highly ordered Fe_3Mn supercell [Fig. 1(a)] and also lower than diffusion paths along chains of Fe atoms in the same supercell. We, therefore, further conclude that Mn percolation chains act as preferred (i.e., fast) diffusion channels for interstitial hydrogen.

To quantify the impact of the Mn percolation chains on the H mobility, we have determined the diffusion rate of H interstitials for such an atomic configuration employing KMC. Using Eq. (4) and the computed *ab initio* barriers, the

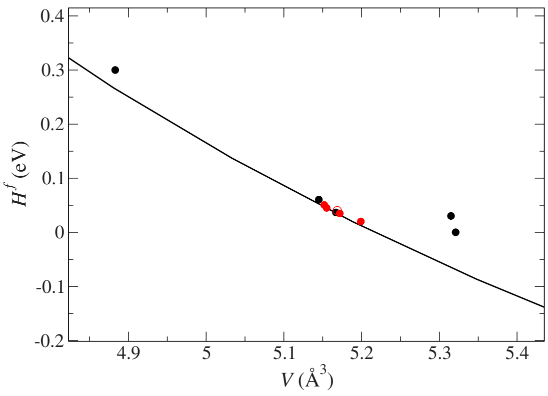

FIG. 5. (Color online) Correlation between the solution enthaply H^f_σ and the Voronoi interstitial volume V. The filled (empty) red points mark results for the various octahedral sites indicated in Fig. 1 for the Fe_3Mn alloy with (without) Mn percolation chains. The black points mark the results for the five symmetry-inequivalent octahedral interstitial sites in a $Fe_{32}C$ supercell. The black line shows the result for Fe bulk.

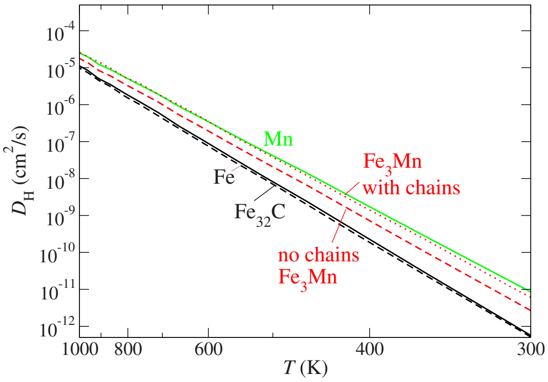

FIG. 6. (Color online) Diffusion rates $D_H = a_{lat}^2 \Gamma$ determined with the KMC technique. The highly ordered Fe_3Mn alloy without chains [dashed red line, Fig. 1(a)] and the alloy with Mn percolation chains [dotted red line, Fig. 1(b)] are given. Further, results for the $Fe_{32}C$ supercell (dashed black line) is simulated. For comparison, the results for pure fcc Fe (black line) and Mn (green, light line) are included.

master Eq. (5) is constructed and solved. The KMC simulations included all inequivalent tetrahedral and octahedral sites, as well as all 256 diffusion barriers in between, as obtained from the 3D PES. As result we obtain temperature-dependent diffusion rates $D_H(T)$ for the disordered Fe_3Mn alloy where the Mn percolation chains are present. The resulting diffusion rate is shown in Fig. 6 and compared with pure Fe ($E^{diff} = 0.62$ eV) and pure Mn ($E^{diff} = 0.55$ eV). The effective diffusion barrier as defined by Eq. (6) is 0.56 eV. This value is much closer to pure Mn than to pure Fe. The reduction in the Mn diffusion barriers due to the presence of Mn percolation chains becomes also apparent in a direct comparison with the ordered Fe_3Mn alloy, where $E^{diff} = 0.58$ eV. While the differences are small compared to the absolute diffusion barrier, they result in a room-temperature change in the transition rate of approximately 1 order of magnitude (see Fig. 6) and make the diffusion in an Fe_3Mn alloy almost as efficient as in a pure Mn crystal.

C. Effect of interstitial carbon

Carbon is another important alloying element in TRIP and TWIP steels that may alter the diffusion rate of interstitial H. Typical C concentrations in these steels are ≈ 3 at. %, which we simulate by a $Fe_{32}C$ supercell. Checking various interstitial sites, we find the octahedral one to be most stable. This result is consistent with a previous study.[24] Incorporating C into the supercell has two effects: (i) it causes an appreciable lattice expansion of 0.04 Å (approximately 1% of the Fe lattice constant) and (ii) it breaks the symmetry of the host lattice, leaving five symmetry-inequivalent octahedral interstitial sites with different hydrogen-solution enthalpies. Three of the octahedral sites (O_2, O_4, and O_5 in Fig. 7) have a lower solution enthalpy than in the unperturbed Fe lattice. For the most favorable octahedral site (O_5), the reduction in the solution enthalpy is 0.06 eV.

To analyze the origin of the large variations in the H-solution enthalpies, we computed again the interstitial volume of all octahedral sites in the $Fe_{32}C$ supercell using a Voronoi construction. Like for the pure Fe and the Fe_3Mn alloys, the volume-energy pairs have been included in Fig. 5. As can be seen there, the data points again closely follow the (H^f, V) curve of a strained, pristine Fe lattice. Since also the data points for the FeMn cells are located on this curve, we conclude that it describes a universal trend of the Fe-Mn-C system. The local solution enthalpy for hydrogen does not explicitly depend on the local composition and configuration of the host matrix but is to a major part determined by the local interstitial volumes.

The effect of interstitial C on the hydrogen mobility is summarized in Fig. 7. As can be seen, in planes where interstitial C atoms are present, the H diffusivity is reduced compared to the Fe bulk. In contrast, planes which do not contain interstitial C exhibit an increased H diffusivity and hence serve as diffusion channels. To determine the effective change in the overall mobility of hydrogen due to the presence of intersitial C, we have performed again a KMC simulation. The underlying master equation has been constructed using the energies for all 64 tetrahedral (four of which are symmetrically inequivalent) and for all 32 (five inequivalent) octahedral and all 256 (nine inequivalent) diffusion barriers as obtained from the DFT calculations. As a result, we obtained the temperature-dependent diffusion rates $D_H(T)$. The effective diffusion barrier, given by Eq. (6), for the considered $Fe_{32}C$ supercell differs from the barrier in the unperturbed Fe lattice by less than 10 meV. This implies that the diffusion of H is basically not affected by the presence of C. This is a remarkable result since common belief is that C intersitials act as trapping centers for interstitial hydrogen, i.e., they are expected to decrease the net H-diffusion rates.

We note, however, that this conclusion holds strictly only for the considered supercell. In more realistic situations, C atoms are distributed randomly rather than in the highly ordered arrangement imposed by the supercell. Nevertheless, for similar concentrations, the qualitative character of the lattice strain will not be affected by the particular configuration of the C atoms. The solution enthalpy is lowered with respect to the unperturbed lattice since there will always be interstitial sites with a larger volume than in pure Fe whereas the diffusion constant of H will experience less changes, due to the averaged compensation of regions with compressive and tensile strain.

D. Effect of magnetism and zero-point vibrations

The energy differences of the volumetric trends identified above are on the order of 0.1 eV. Further effects, such as zero-point vibrations and magnetism, might result in corrections of the same order of magnitude and need therefore to be considered.

Quantum-mechancial ZPVs are particularly important in the case of H since it is the lightest chemical element. We have therefore determined its value for hydrogen in Mn and in Fe (for technical details see Sec. II). For both systems, we find significant corrections to the solution enthalpy, being as large as $H^{f,ZPV} = 0.07$ eV for Fe and $H^{f,ZPV} = 0.09$ eV for Mn. Hence, we conclude that taking these corrections into

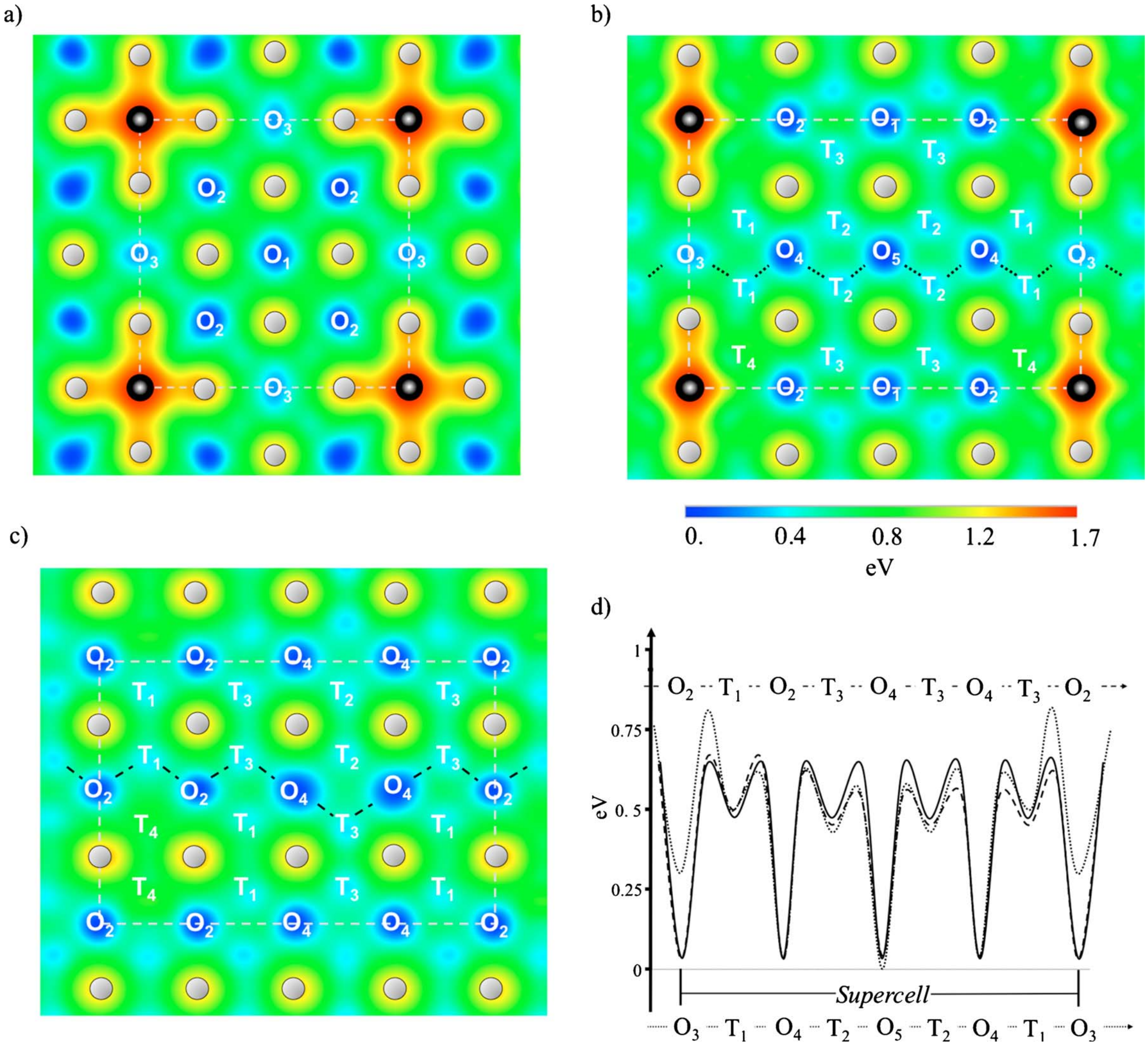

FIG. 7. (Color online) Potential-energy surface (schematic, colored) for placing a hydrogen atom in a $Fe_{32}C$ supercell: (a) along the [100] plane, (b) along the [110] plane containing the C impurities, and (c) along the [100] plane shifted by one layer from the C impurities. The dark (light) balls denote the positions of the C (Fe) atoms. The octahedral (tetrahedral) interstitial lattice sites are labeled O_x (T_x). The dotted and dashed lines denote specific paths for hydrogen diffusion. (d) Solution enthalpies and energy barriers along the dotted ($O_3 \cdots T_1 \cdots O_4 \cdots T_2 \cdots O_5 \cdots T_2$) and the dashed ($O_2 \cdots T_1 \cdots O_2 \cdots T_3 \cdots O_4 \cdots T_3$) path marked in (b) and (c), respectively. Visualization of the solution enthalpies and energy barriers along these paths, as provided in the table. All energies are in electron volt and taken with respect to the lowest-energy position for H and the O_5 octahedral site.

account is crucial to obtain accurate *absolute* values for the solution enthalpies at $T=0$ K. For chemical trends, however, only *differences* in solution enthalpies and diffusion barriers enter. A rough upper limit of the ZPV is obtained when considering the two extreme cases for $Fe_{1-x}Mn_x$ alloys ($x=0$ and $x=1$). The differences in the ZPV are only 0.02 eV. Assuming a linear relationship of the ZPV differences with the alloy concentration, this difference becomes for the Fe_3Mn ($x=0.25$) alloy considered here less than 10 meV and will therefore not affect any of the trends identified above.

The magnetic order of the host matrix may have an impact on the solubility and mobility of hydrogen since it results in an induced magnetic moment at the H atom. Further, for Fe and FeMn alloys, strong magnetovolume effects are characteristic. For austenitic steels, investigated in this study, the magnetic structure is known to be complex. Experimental observations[31] confirmed by first-principles noncollinear-spin calculations[32,33] showed a spin-spiral magnetic ground state for fcc Fe. Also Mn and FeMn alloys are reported to have noncollinear spin-spiral magnetic ground states.[34] However, at elevated temperatures, an antiferromagnetic order is experimentally reported, with Néel temperatures around 400 K in the considered high Mn alloys (see Ref. 35, and references therein). In order to understand/estimate the importance of magnetic effects on H solubility and diffusion, we will consider in the following three configurations: the nonmagnetic (NM) state, the ferromagnetically ordered state in the high-spin (FMHS) configuration, and the antiferromagnetic double-layer ordering (AFMD). The latter has been shown in previous DFT calculations to be the energetically most stable collinear configuration at $T=0$ K and to provide a good approximation of the true noncollinear ground state in γ Fe.[36]

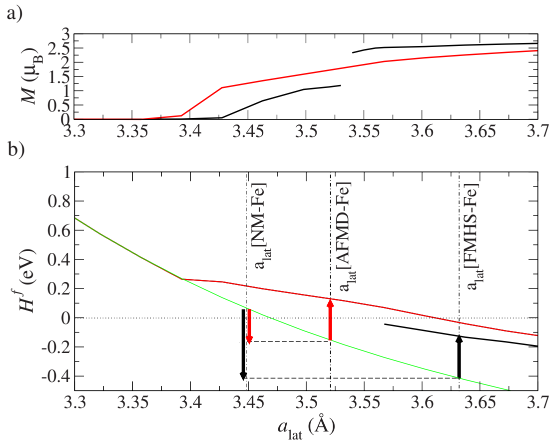

FIG. 8. (Color online) (a) Local magnetic moments in bulk fcc Fe in the ferromagnetic (FM) phase (black line) and the antiferromagnetic double-layer phase (red line). (b) H-solution enthalpy in nonmagnetic (NM, green, light line), ferromagnetic (FM, black line), and antiferromagnetic double-layer Fe (AFMD, red line), plotted as a function of the lattice constant. For the ferromagnetic phase, the solution enthalpies are only plotted for lattice constants >3.6 Å, corresponding to the FMHS domain since for smaller values, the FM phase becomes unstable and the magnetic structure relaxes to the AFMD phase, when the H atom is introduced into the Fe matrix. Downward pointing arrows denote the indirect volumetric effect whereas upward pointing arrows denote the direct effect the magnetism has on the solution enthaply (see main text).

The results are summarized in Fig. 8. As can be seen, switching on magnetism yields two competing effects: a first, *indirect* effect is the increase in the lattice constant with increasing magnetic order (NM → AFMD → FM). This effect results in larger interstitial volumes and hence a lowering of the H-solution enthalpies. The change induced by this effect is marked by the downward pointing arrows in Fig. 8. It amounts to an energy difference to the NM state of 0.50 eV at the lattice constant of the FM-HS phase and 0.23 eV at the lattice constant of the AFMD phase. A second, *direct* effect is a repulsion of the hydrogen atoms by the magnetic moments. This can be seen by the fact that switching on magnetism significantly raises the H formation enthalpy, i.e., lowers the H-solution enthalpy. We therefore conclude that the hydrogen interstitial prefers a nonmagnetic environment. This effect is marked by the upward pointing arrows in Fig. 8. It amounts to 0.28 eV for the FM phase with local magnetic moments of $2.5\mu_B$ and to 0.29 eV for the AFMD phase with local magentic moments of $2.1\mu_B$. Both, the direct and the indirect effect caused by magnetism are large on the energy scale we are interested in. However, since they have opposite signs, they largely compensate each other. The overall correction for the AFMD phase amounts to only 50 meV. Corrections for the relative differences between $Fe_{1-x}Mn_xC_y$ and pure Fe are expected to be even smaller and to have therefore no relevant influence on the qualitative chemical trends derived here.

Adding the zero-point vibrational corrections $H^{f,\mathrm{ZPV}}=0.07$ eV to the solution enthalpy corresponding to the value for the AFMD magnetic structure, $H^{f,\mathrm{AFMD}}=0.13$ eV, yields for the corrected solution enthalpy $H^{f,\mathrm{AFMD,ZPV}}=0.20$ eV. A direct comparison of these values with experimental values for the solution enthalpy (as provided, e.g., in Ref. 37, and references therein) has to be taken with care since these experiments can only be performed in the stability range of the γ phase of iron, i.e., between 900 and 1400 K. In experimental studies, H^f is determined as the slope of the logarithmic plot of the solubility vs $1/T$. These studies report values between 0.23 and 0.28 eV, which are slightly larger than our value by about 0.03–0.08 eV. Remaining uncertainties of this order can be attributed to the approximate description of magnetic effects in our approach.

IV. CONCLUSIONS

Combining DFT-computed potential-energy surfaces and kinetic Monte Carlo, we have studied and analyzed the solubility and kinetics of interstitial hydrogen in pure and carbon-containing FeMn alloys. Our results show that Mn increases both the solubility and the mobility of H. Based on a detailed analysis of the various energy contributions, we could show that these higher values are a volume effect. Using the Voronoi method as a measure of the interstitial volume that can be occupied by a single H atom, we find an almost linear relation with respect to solution enthalpy and diffusion barrier. For the alloy system considered here, this relation is almost independent of the specific chemistry. Thus, the larger mobility and solubility when increasing the Mn content is dominated by the volume expansion induced by the larger atomic radius of Mn compared to that of Fe. The slope and the magnitude of the linear relation are found to be surprisingly robust and apply even to strong local fluctuations as induced, e.g., around C impurities or due to Mn chains.

These observations have interesting consequences. First, for Mn concentrations above 20%, where according to percolation theory long-range Mn chains are present, diffusion along the chains is found to be almost as efficient as in a pure fcc Mn crystal. Second, in contrast to conventional wisdom, C at concentrations of ≈3 at. % acts not as a trap slowing down diffusion. Instead, regions with compressive and tensile strain largely cancel, resulting in a net diffusion that is almost identical to that of the pure crystal. Third, due to the volume relation the change in the H energetics caused by different magnetic configurations is partially compensated by induced changes in the lattice constants, allowing to estimate the properties of H in computationally less demanding nonmagnetic calculations. Finally, we note that the significantly increased mobility of H in FeMn alloys above the percolation limit may be related to the higher vulnerability of these steels with respect to H embrittlement.

ACKNOWLEDGMENTS

The authors gratefully thank ThyssenKrupp Steel Europe for the cooperation and the funding of the project. Special thanks go to R. Großterlinden, H. Hofmann, and T. Pretorius for fruitful discussions and comments. Furthermore, the support of J. von Pezold is greatly appreciated.

*ismer@engineering.ucsb.edu

†hickel@mpie.de

[1] G. Frommeyer and U. Brüx, Steel Res. Int. **77**, 627 (2006).

[2] S. Allain, J. P. Chateau, and O. Bouaziz, Mater. Sci. Eng., A **387-389**, 143 (2004).

[3] G. Frommeyer, U. Bruex, and P. Neumann, ISIJ Int. **43**, 438 (2003).

[4] O. Grässel, L. Küger, G. Frommeyer, and L. W. Meyer, Int. J. Plast. **16**, 1391 (2000).

[5] Y. Tomota, M. Strum, and J. W. Morris, Metall. Trans. A **17**, 537 (1986).

[6] Y. G. Kim, J. M. Han, and J. S. Lee, Mater. Sci. Eng., A **114**, 51 (1989).

[7] W. Godoi, N. K. Kuomoto, A. S. Guimaraes, and C. M. Lepienski, Mater. Sci. Eng., A **354**, 251 (2003).

[8] H. Uhlig, Trans. Am. Inst. Min., Metall. Pet. Eng. **158**, 183 (1944).

[9] S. Mittal, R. C. Prasad, and M. B. Deshmunkh, ISIJ Int. **35**, 302 (1995).

[10] S. Fukuyama, D. S. Sun, L. Zhang, M. Wen, and K. Yokogawa, J. Jpn. Inst. Met. **67**, 456 (2003).

[11] L. W. Tsay, S. C. Yu, and R.-T. Huang, Corros. Sci. **49**, 2973 (2007).

[12] E. A. Steigerwald, F. W. Schaller, and A. R. Troiano, T. Am. I. Min. Met. Eng. **218**, 832 (1960).

[13] A. Inoue, Y. Hosoya, and T. Masumoto, Trans. Iron Steel Inst. Jpn. **19**, 170 (1979).

[14] H. K. Birnbaum and P. Sofronis, Mater. Sci. Eng., A **176**, 191 (1994).

[15] T. Michler and J. Naumann, Int. J. Hydrogen Energy **33**, 2111 (2008).

[16] *Environmental Degradation of Enegineering Materials in Hydrogen*, edited by G. R. Caskey, M. R. Louthean, R. F. McNitt, and R. D. Sisson (Virginia Polytechnical Institute, Blacksburg, VA, 1981).

[17] C. S. Marchi, B. P. Somerday, X. Tang, and G. H. Schiroky, Int. J. Hydrogen Energy **33**, 889 (2008).

[18] V. G. Gavriljuk, V. N. Shivanyuk, and J. Foct, Acta Mater. **51**, 1293 (2003).

[19] Y. Tan, D. H. Zhou, and J. Feng, Acta Metall. Sin. (Engl. Lett.) **10**, 228 (1997).

[20] C. S. Becquart, C. Domain, and J. Foct, Philos. Mag. **85**, 533 (2005).

[21] C. Domain, C. S. Becquart, and J. Foct, Phys. Rev. B **69**, 144112 (2004).

[22] S. Simonetti, M. E. Pronsato, G. Brizuela, and A. Juan, Phys. Status Solidi B **244**, 610 (2007).

[23] T. Yu, L.-Q. Chen, C.-Y. Wang, Z.-C. Qiu, and J.-P. Du, Chin. Sci. Bull. **53**, 1796 (2008).

[24] D. E. Jiang and E. A. Carter, Phys. Rev. B **67**, 214103 (2003).

[25] S. M. Teus, V. N. Shivanyuk, B. D. Shanina, and V. G. Gavriljuk, Phys. Status Solidi A **204**, 4249 (2007).

[26] J. P. Perdew, J. A. Chevary, S. H. Vosko, K. A. Jackson, M. R. Pederson, D. J. Singh, and C. Fiolhais, Phys. Rev. B **46**, 6671 (1992).

[27] P. E. Blöchl, Phys. Rev. B **50**, 17953 (1994).

[28] G. Kresse and J. Furthmüller, Phys. Rev. B **54**, 11169 (1996).

[29] C. Lorenz and R. Ziff, J. Phys. A **31**, 8147 (1998).

[30] This energy difference is small and smaller/comparable to the thermal energy ($k_{\mathrm{B}}T$) where the local structure in the austenite is frozen in. The distribution of the Mn atoms in the steel matrix is therefore entropy rather than energy driven, resulting in a disordered structure consistent with experimental observations and with the formation of percolation chains.

[31] Y. Tsunoda, J. Phys.: Condens. Matter **1**, 10427 (1989).

[32] O. N. Mryasov, A. I. Liechtenstein, L. M. Sandratskii, and V. A. Gubanov, J. Phys.: Condens. Matter **3**, 7683 (1991).

[33] M. Körling and J. Ergon, Phys. Rev. B **54**, R8293 (1996).

[34] S. Fujii, S. Ishida, and S. Asano, J. Phys. Soc. Jpn. **60**, 4300 (1991).

[35] V. T. Witusiewicz, F. Sommer, and E. J. Mittemeijer, Metall. Mater. Trans. B **34**, 209 (2003).

[36] E. Sjöstedt and L. Nordström, Phys. Rev. B **66**, 014447 (2002).

[37] A. San-Martin and F. D. Manchester, Bull. Alloy Phase Diagrams **11**, 173 (1990).